Pattern Recognition 87 (2019) 38–54

disturbances, and noises in XCA images. Because the contrast-filled vessels have different motion patterns for the contrast-filled vessels and background structures, they include the vessel layer or foreground layer, whereas all other structures are called background layer. Due to the complex dynamic structures, the background layer seriously disturbs the observation and measurement of vessels. To facilitate the diagnosis and treatment of cardiovascular diseases, automatical extraction of the vessel layer and effective removal of the nonvascular background layer has become a prerequisite to improve the visibility and detection of vessels for various clinical applications, such as 3D reconstruction of coronary arteries [12], 3D/2D image coronary registration [13], coronary artery labeling [14], heart's dynamic information extraction [15], and myocardial perfusion measurement [4,5,16]. In addition, vessel extraction is usually used as a preprocessing step to remove noises and complex backgrounds from XCA images while emphasizing vessel-like structures for most sophisticated pipeline algorithms including vessel segmentation and vessel centerline extraction.

Currently, most vessel extraction methods mainly focus on removing background noises and improving the saliency of vessels. While vessel structures can be highlighted, the vessel intensity information in the images is neglected and lost after the processing steps with previous methods. A more accurate vessel layer extraction with structure and intensity recovery will definitely facilitate further quantitative analysis of

Decomposition (t-SVD) [48,49], has been verified effective for 3D tensor completion [50,51]. Hu et al. have further optimized the TNN model for the video completion task by integrating a twist operation [52].

1.3. Overview and contributions

Existing layer separation works share a similar global strategy for layer modeling, *i.e.*, these methods treat an XCA image as a whole, and aim to directly separate layers from all the pixels. Under this strategy, the intensity of every pixel in an XCA image has a potential to be split up into several parts. As a result, local interaction of different layers will affect the global separation. Specifically, popular RPCA methods have the following three main limitations for foreground/background separation in XCA images. First, vectorizing the XCA video sequence into a matrix makes the RPCA model ignore the 3D spatio-temporal information between the consecutive frames of the XCA sequence. For example, X-ray imaging produces a lot of dense noisy artifacts, whose positions change in a gradually moving pattern in the XCA frames. The RPCA methods often recognize these moving artifacts as foreground objects.

The second limitation is that most RPCA-based image decomposition imposes the foreground component being pixel-wisely sparse (e.g., L_1-norm for the sparsity) and the background component being globally low-rank without locally considering the complex spatially varying noise in observation data. However, an observation of low dose X-ray imaging is not only badly corrupted by spatially varying signal-dependent Poisson noise [53,54], but also of low contrast and low SNR between the noise and the signal. This serious signal-dependent noise locally affects every entry of the data matrix and results in unsatisfying foreground vessel images containing many artifact residuals. Though Bayesian RPCA modeling data noise as a mixture of Gaussians is developed [55] to fit a wide range of noises such as Laplacian, Gaussian, sparse noise and any combinations of them, or GoDec+ [56] introduces a robust local similarity measure called correntropy to describe the data corruptions including Gaussian noise, Laplacian noise, and salt & pepper noise on real vision data, these methods cannot tackle the challenging problem of spatially varying noise in low-rank and sparse decomposition. To further remove these spatially varying noisy artifacts from the low contrast foreground vessel, the importance of vessel details in the foreground image sequences should be highlighted. Recently, reducing noise while preserving the visually important image details have attracted increasing attention in .

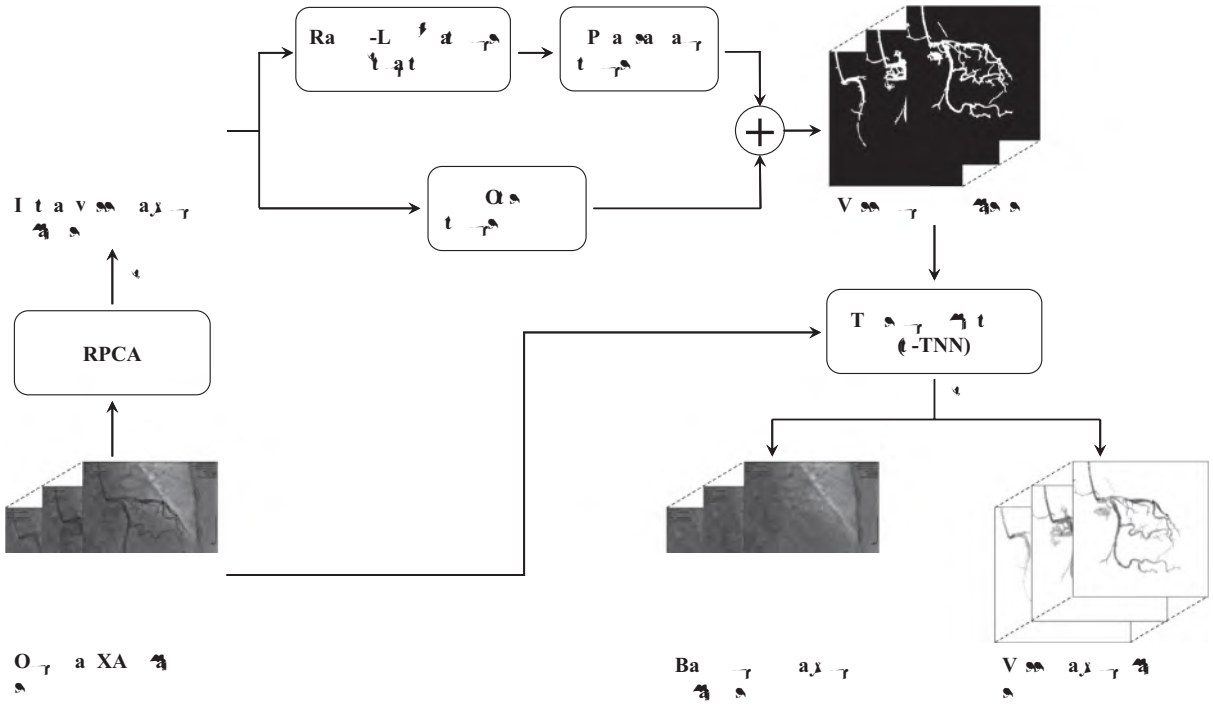

Fig. 1. Overview of VRBC-t-TNN for an XCA image sequence.

complete the low-rank background layers that are then subtracted from the overall XCA images. Therefore, both the structures and the intensities of vessels are well recovered with the proposed method.

2. Methods

2.1. Overview

The proposed vessel layer extraction method called VRBC-t-TNN contains three main procedures. First, the vessel mask regions are extracted by combining the RPCA algorithm [60] with a vessel feature filtering based segmentation method [27]. As a preprocessing step of RPCA, a global logarithm transformation is performed on the input XCA sequence to create the X-ray attenuation sum model for the subsequent vessel/background decomposition. By exploiting the sparse outlier property of moving contrast in vessel regions and eliminating the disturbance of background structures, the initial contrast-filled vessel layer is extracted from the X-ray attenuation data by RPCA algorithm [60]. The vessel regions are then segmented out from the initial vessel layers via joint enhancement and denoising strategy that is implemented by RLF filtering and spatially adaptive thresholding. Secondly, the whole background layers are completed by completing the vessel-overlapped background regions based on neighboring background pixel information via a tensor completion algorithm called t-TNN [52]. Finally, the vessel layers are accurately extracted via subtraction of all the background layers from the whole attenuation data. Fig. 1 provides an overview of the whole procedure. Details are described in the remaining part of Section 2.

2.2. Global intensity mapping

A global logarithm mapping is carried out on the whole XCA image data to perfectly fit the X-ray attenuation sum model of angiograms. In X-ray imaging, photons coming through human body are attenuated by contrast agents and various human tissues. The intensity of rays is reduced exponentially by the sum of attenuation coefficients, as the following equation:

$$X_{out} = X_{in} e^{-\int_d \mu dx}, \tag{1}$$

where X_{in} and X_{out} represent the intensities of X-rays that come into and out of human body, respectively, μ denotes the attenuation coefficient, d denotes the path of rays.

By applying the log operator on both sides, we get:

$$-\ln(X_{out}/X_{in}) = \int_d \mu dx. \tag{2}$$

The XCA image intensity normalized to the range [0, 1] can be regarded as the normalization of the ray intensity, *i.e.* the ratio of X_{out} to X_{in}. Then we get the following equation:

$$-\ln(I_{XCA}) = -\ln(X_{out}/X_{in}) = \int_{d_1} \mu dx + \int_{d_2} \mu dx = A_F + A_B, \tag{3}$$

where A_F and A_B represent the attenuation sums caused by foreground vessels and complex backgrounds, respectively. Eq. (3) demonstrates that the XCA image is a sum of vessel/background layers in the logarithm domain, accordingly the multiplication of the two layers in the original image domain.

After this logarithm mapping, the linear sum model of Eq. (3) is ready for vessel/background separation via low-rank plus sparse matrix decomposition in RPCA (Illustrated in Section 2.3), as well as low-rank background plus foreground vessel extraction in tensor completion (Illustrated in Section 2.5). Therefore, we use the logarithm operation as a preprocessing of image data and perform exponentiation operation afterwards for the whole experiments in this work.

2.3. Preliminary vessel layer extraction

Though vessels can be segmented directly from original XCA images, the complex background structures and spatially varying noises may bring too many noisy artifacts into the segmentation results. Therefore, in this step an initial vessel layer with reduced background structures is preliminarily extracted from the XCA attenuation data sequence for better vessel segmentation. The XCA

attenuation sequence is formed as a matrix D with each frame vectorized as a column. By exploiting the sparse outlier of moving contrast in the vessel layers, the RPCA algorithm is performed on the XCA attenuation data to extract the contrast-filled vessel layer.

The RPCA model [39] minimizes the sum of matrix nuclear norm of background and L_1 norm of foreground component:

$$\min_{L,S} \|L\|_* + \lambda \|S\|_1, \ s.t. \ D = L + S, \tag{4}$$

where $D \in \mathbb{R}^{n_1 \times n_2}$ denotes the data matrix, $L \in \mathbb{R}^{n_1 \times n_2}$ and $S \in \mathbb{R}^{n_1 \times n_2}$ denote the low-rank component (background layer) and the sparse component (foreground layer), respectively, λ is a positive weighting parameter, $||S||_1 = \sum_{i,j} |S_{i,j}|$ is the L_1 norm, $\|L\|_*$ denotes the nuclear norm of L, which is an approximation to the matrix rank. The nuclear norm in Eq. (4) tightly couples all samples in the image sequence. This RPCA model has been proven efficient in moving object detection, including vessel

Algorithm 2 Vessel segmentation.

Input: Initial vessel layer image I_{iv} (a frame of S from Algorithm 1).

1: Otsu threshold all I_{iv}s to get binary mask M_Os;
2: Calculate the Radon-Like features of I_{iv}, the resulted RLF image is denoted by R_{iv};
3: Phansalkar threshold R_{iv} to get mask M_P;
4: Remove regions smaller than a fixed size t_s from M_P;
5: Take the foreground pixels in M_P as seeds, do conditional dilation in M_O, the result mask image is denoted by M_c;
6: Merge the foreground regions in M_P and M_c together to get the final mask image M_V.

Output: Binary vessel mask image, M_V.

methods. After testing several algorithms, we adopt the t-TNN algorithm [52] that can exploit the temporal redundancy and low-rank prior between the neighboring frames more efficiently than other tensor completion algorithms. The original XCA sequence is formed as a tensor $\mathcal{D}$ with each slice being a matrix representation of each frame. All areas except the vessel mask regions, denoted as Ω, are presumed to be the known background layer pixels. To make sure that Ω does not contain edge pixels of the vessels,e Tm .0001 Tc ((eac)10.7(h)]TJ /F2 1 Tf 6.3761 0 0 6.3761 89.1457 523.0 7.9701 28)Tj /F1 1 Tf 7.9701 0 0 7.9701 61.31 8]TJ3.70 Tm .0

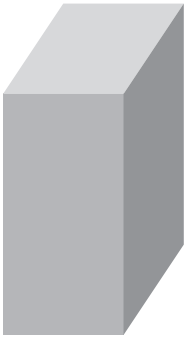

The whole procedure of the t-TNN background completion step is shown in Algorithm 3.

3. Experimental results

3.1. Real and synthetic XCA data

In this work, we used two types of experimental data for the evaluation of VRBC-t-TNN: real clinical XCA data and synthetic XCA data. All the 12 sequences of real XCA images are obtained from Ren Ji Hospital of Shanghai Jiao Tong University. Each sequence contains 80 frames whose image resolution is 512×512 pixels with 8 bits per pixel. All the experiments in this paper were approved by our institutional review board.

To accurately evaluate the vessel region and intensity recovery, we constructed 10 sequences of synthetic XCA images with ground truth background layer images (GTBL) and vessel layer images (GTVL). To get GTVLs, we perform vessel extraction similar to Algorithms 1 and 2 described in Section 2 with slightly different parameters on the real XCA data. Then we remove some artifacts manually from the extracted rough vessel images to obtain the GTVLs. The GTBLs are the consecutive frames selected from the real XCA data. Because a XCA image is the product of the vessel layer and the background layer according to the X-ray imaging mechanism (see Section 2.2), we multiply a sequence of GTVLs to the clean regions of GTBLs from a different sequence to obtain the synthetic XCA data. An example synthetic image with GTBL and GTVL is shown in Fig. 7

visibility.49(9701 0 0 7.9701161.1678 413.613 T537/505951.36347524.g)Tj /F2 1 Tf 6.3761 0 0 6.37

Fig. 4. Vessel mask images by different vessel segmentation methods. Segmentation results of four XCA images are shown in four rows. From left to right, each row displays the original XCA image, the manually outlined ground truth vessel mask, the images processed by Frangi's, Coye's, Felfelian's method, MSRG, CNN-Xray, Retina-unet, and the proposed method, respectively.

images of VRBC-t-TNN achieve the best visual performances. Both the background layer images and the vessel layer images are visually appealing and seem to be well recovered 002 Tc [(la)14.6(y)24.3(e)0(r)]TJ /F2 1 Tf 8(r)8 0 TD 0 Tc ( )Tj /F1 1 Tf .3585 0 TD .0003 Tc [(imag

Fig. 5. Example 1 of vessel layer extraction results from real data. Each group of results contains a background layer image labeled 1 and a vessel layer image labeled 2. (a) Original XCA image. (b)–(l) Layer separation results: (b) MedSubtract. (c) PRMF. (d) MoG-RPCA. (e) IALM-RPCA. (f) MCR-RPCA. (g) VRBC-PG-RMC. (h) VRBC-MC-NMF. (i) VRBC-ScGrassMC. (j) VRBC-LRTC. (k) VRBC-tSVD. (l) VRBC-t-TNN.

Table 1
The average detection rate, precision, F-measure (mean value ± standard deviation) for all methods using the real and synthetic data.

	Real			Synthetic
Method	DR	P	F	DR
Frangi's	0.529 ±0.244	0.272 ±0.114	0.352 ±0.144	0.558 ±0.199
Coye's	0.703 ±0.109	0.318 ±0.113	0.422 ±0.108	0.671 ±0.186
Felfelian's	0.715 ±0.178	0.511 ±0.166	0.560 ±0.124	0.412 ±0.273
MSRG	0.549 ±0.235	0.752 ±0.125	0.597 ±0.193	0.425 ±0.175
CNN-Xray	0.547 ±0.195	0.834 ±0.076	0.636 ±0.162	0.744 ±0.083
Retina-Unet	0.571 ±0.196	0.457 ±0.096	0.491 ±0.131	0.782 ±0.135
Proposed	**0.773 ±0.050**	0.704 ±0.126	**0.729 ±0.067**	**0.888 ±0.048**

3.6. Quantitative evaluation on vessel intensity recovery using synthetic data

To measure the accuracy of vessel intensity recovery, we directly calculated the differences between the extracted vessel layers and the ground truths. The reconstruction error of vessels is defined as follow:

$$E_{recon} = \frac{\sum_{(x,y)\in V} |I_{result}(x,y) - I_{groundtruth}(x,y))|}{\sum_{(x,y)\in V} I_{groundtruth}(x,y)}, \tag{21}$$

where V denotes the vessel regions, I_{result} and $I_{groundtruth}$ denote the intensities of the resulting vessel layer images and the ground truth vessel layer images, respectively. For each synthetic XCA sequence, the E_{recon} of the whole sequence is calculated. Fig. 10 and Table 3 show the general performances of different algorithms on the 10 synthetic sequences.

E_{recon} measures the vessel intensity difference between the separation result and the ground truth. A small E_{recon} indicates an accurate vessel layer extraction. We can see that VRBC achieves smaller E_{recon} values than other existing methods. Among them, VRBC-t-TNN achieves the best performance. This E_{recon} evaluation indicates that VRBC-t-TNN can accurately recover the contrast-filled vessel intensities from XCA images.

Fig. 6. Example 2 of vessel layer extraction results from real data. Each group of results contains a background layer image labeled 1 and a vessel layer image labeled 2. (a) Original XCA image. (b)–(l) Layer separation results: (b) MedSubtract. (c) PRMF. (d) MoG-RPCA. (e) IALM-RPCA. (f) MCR-RPCA. (g) VRBC-PG-RMC. (h) VRBC-MC-NMF. (i) VRBC-ScGrassMC. (j) VRBC-LRTC. (k) VRBC-tSVD. (l) VRBC-t-TNN.

Table 2
The average CNR values (mean value ± standard deviation) for all methods using the real data.

Method	Global CNR	Local CNR
Original	1.026 ± 0.345	1.558 ± 0.500
MedSubtract	5.074 ± 2.035	6.475 ± 3.109
PRMF	6.869 ± 2.461	8.955 ± 3.690
MoG-RPCA	6.941 ± 2.518	8.959 ± 3.644
IALM-RPCA	8.323 ± 2.974	9.909 ± 3.485
MCR-RPCA	9.898 ± 4.016	12.252 ± 5.094
VRBC-PG-RMC	11.266 ± 8.214	9.078 ± 3.245
VRBC-MC-NMF	11.098 ± 6.367	9.710 ± 4.149
VRBC-ScGrassMc	12.197 ± 6.848	10.700 ± 4.879
VRBC-LRTC	11.846 ± 9.199	9.717 ± 3.649
VRBC-tSVD	14.842 ± 9.887	11.722 ± 4.643
VRBC-t-TNN	**14.976** ± **9.961**	**12.083** ± **4.789**

Table 3
The average E_{recon} values (mean value ± standard deviation) for all methods using the 10 synthetic sequences.

Method	E_{recon}
MedSubtract	0.073 ± 0.012
PRMF	0.053 ± 0.009
MoG-RPCA	0.055 ± 0.012
IALM-RPCA	0.050 ± 0.009
MCR-RPCA	0.061 ± 0.010
VRBC-PG-RMC	0.039 ± 0.006
VRBC-MC-NMF	0.045 ± 0.006
VRBC-ScGrassMc	0.041 ± 0.007
VRBC-LRTC	0.037 ± 0.006
VRBC-tSVD	0.033 ± 0.005
VRBC-t-TNN	0.030 ± 0.005

3.7. Computation times

Finally, we report on the computation costs incurred by our VRBC-t-TNN algorithm on a Lenovo PC equipped with an Intel Core i5-4460 Quad-Core 3.2 GHz CPU and 8 GB of RAM executing Matlab codes. The average processing time of a $512 \times 512 \times 80$ real XCA sequence is approximately 970 s. The RPCA step, vessel filtering step and t-TNN step take approximately 28 s, 740 s and 200 s, respectively.

4. Discussion and conclusion

We have presented a new low-rankness based decomposition framework for accurate vessel layer extraction from XCA image sequences. By constructing the background layer via tensor completion of the vessel regions from original XCA images, the proposed method can overcome limitations in current vessel extraction methods and has significantly improved the accuracy of vessel intensity recovery with enhanced vessel visibility. In this method, the raw XCA image sequences are first mapped into

Fig. 7. Examples of vessel layer extraction results from synthetic data. Each group of results contains a background layer image labeled 1 and a vessel layer image labeled 2. (a–0) Synthetic XCA image. (a–1,2) Ground truth background layer and vessel layer image. (b)-(l) Layer separation results: (b) MedSubtract. (c) PRMF. (d) MoG-RPCA. (e) IALM-RPCA. (f) MCR-RPCA. (g) VRBC-PG-RMC. (h) VRBC-MC-NMF. (i) VRBC-ScGrassMC. (j) VRBC-LRTC. (k) VRBC-tSVD. (l) VRBC-t-TNN.

a logarithmic domain to perfectly fit the X-ray attenuation sum model along the vessel and background layers into the subsequent vessel/background decomposition modeling. We subsequently use the low-rank and sparse decomposition via RPCA algorithm to extract the contrast-filled vessel regions. RLF filtering and spatially adaptive thresholding are performed on the vessel layer images to segment out vessel masks. An accurate background layer image sequence is then constructed by t-TNN tensor completion by exploiting the spatio-temporal consistency and low-rankness of background tensor from the consecutive background layers. Finally, the vessel layer images are acquired by subtracting the background layer from original XCA images. Experiments have been done to demonstrate the vessel visibility and accuracy of the results.

The efficacy of the proposed vessel and background layer decomposition framework is based on the exact X-ray attenuation sum model via logarithmic mapping of raw XCA images. This mapping gives sense to the gray levels that are linearly dependent on the matter thickness and density in the vessel and background layers. The linear attenuation sum model is then perfectly fitted into the additive model of low-rank background plus sparse foreground decomposition for the vessel/background separation.

Since RPCA is able to detect moving contrast and to weaken the background noise with the further denoising effect of adaptive vessel feature filtering, RPCA coupled with adaptive vessel feature filtering improved the vessel segmentation that is robust to the complex background noise. There is a general concern that RPCA as a preprocessing step might fail to recognize a portion of vessels and thus lead to segmentation leaks in XCA images. In most cases, the RPCA-based vessel enhancement hardly eliminates any vessel parts in the extracted vessel layer images and is actually able to detect more vessel pixels in the subsequent segmentation step. Especially, some vessel pixels that are faded in background noises are

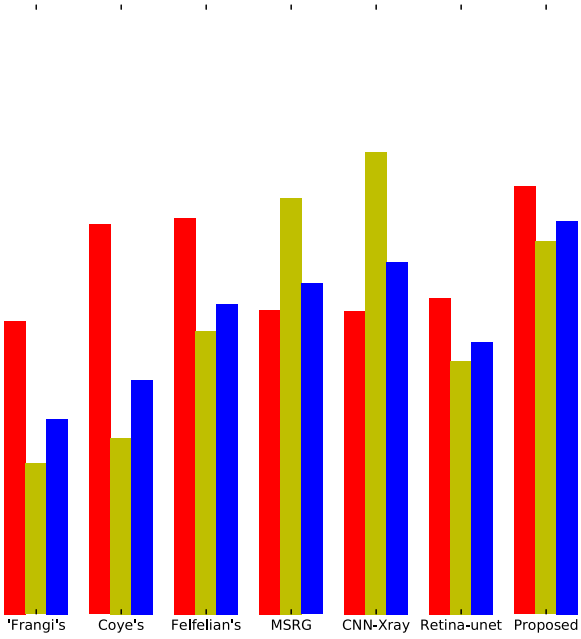
'Frangi's
Coye's
Felfelian's
MSRG
CNN-Xray
Retina-unet
Proposed

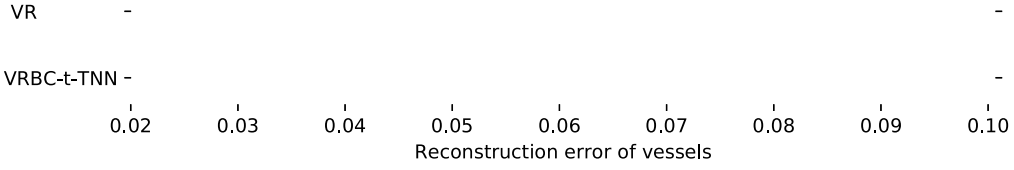
VR
VRBC-t-TNN
0.02
0.03
0.04
0.05
0.06
0.07
0.08
0.09
0.10
Reconstruction error of vessels

In the low-rank and sparse decomposition framework, the successful low-rank background modeling does guarantee the accuracy of foreground vessel extraction. On the one hand, the proposed background modeling with t-TNN-based video tensor completion after segmenting foreground vessel mask regions works better in background modeling than do the other tensor completion algorithms we have tried for this vessel extraction application. We believe that the performance of vessel extraction may be further improved with the development of new tensor completion algorithms. On the other hand, considering that the dynamic real-world background sequences may span one or more

[21] M. Schneider, S. Hirsch, B. Weber, G. Székely, B.H. Menze, Joint 3-D vessel segmentation and centerline extraction using oblique hough forests with steerable filters, Med. Image Anal. 19 (1) (2015) 220–249.
[22] S. Chaudhuri, S. Chatterjee, N. Katz, M. Nelson, M. Goldbaum, Detection of blood vessels in retinal images using two-dimensional matched filters, IEEE Trans. Med. Imag. 8 (3) (1989) 263–269.
[23] Y. Sato, S. Nakajima, N. Shiraga, H. Atsumi, S. Yoshida, T. Koller, G. Gerig, R. Kikinis, Three-dimensional multi-scale line filter for segmentation and visualization of curvilinear structures in medical images, Med. Image Anal. 2 (2) (1998) 143–168.
[24] A.F. Frangi, W.J. Niessen, K.L. Vincken, M.A. Viergever, Multiscale vessel enhancement filtering, in: Proceedings of the International Conference on Medical Image Computing and Computer-Assisted Intervention, 1998, pp. 130–137.
[25] R. Kumar, A. Vázquez-Reina, H. Pfister, Radon-like features and their application to connectomics, in: Proceedings of the IEEE Computer Society Conference on Computer Vision and Pattern Recognition Workshops (CVPRW), IEEE, 2010, pp. 186–193.
[26] T. Syeda-Mahmood, F. Wang, R. Kumar, D. Beymer, Y. Zhang, R. Lundstrom, E. McNulty, Finding similar 2d x-ray coronary angiograms, Med. Image Comput. Comput. Assist. Interv. MICCAI (2012) 501–508.
[27] M. Jin, D. Hao, S. Ding, B. Qin, Low-rank and sparse decomposition with spatially adaptive filtering for sequential segmentation of 2D+t vessels, Phys. Med. Biol. 63 (17) (2018) 17LT01.
[28] W. Zhang, H. Ling, S. Prummer, K.S. Zhou, M. Ostermeier, D. Comaniciu, Coronary tree extraction using motion layer separation, in: Proceedings of the International Conference on Medical Image Computing and Computer-Assisted Intervention, Springer, 2009, pp. 116–123.
[29] Y. Zhu, S. Prummer, P. Wang, T. Chen, D. Comaniciu, M. Ostermeier, Dynamic layer separation for coronary DSA and enhancement in fluoroscopic sequences, in: Proceedings of the International Conference on Medical Image Computing and Computer-Assisted Intervention, Springer, 2009, pp. 877–884.
[30] J.S. Preston, C. Rottman, A. Cheryauka, L. Anderton, R.T. Whitaker, S. Joshi, Multi-layer deformation estimation for fluoroscopic imaging, in: Proceedings of the International Conference on Information Processing in Medical Imaging, Springer, 2013, pp. 123–134.
[31] S. Tang, Y. Wang, Y.W. Chen, Application of ICA to X-ray coronary digital subtraction angiography, Neurocomputing 79 (2012) 168–172.
[32] B. Qin, Z. Gu, X. Sun, Y. Lv, Registration of images with outliers using joint saliency map, IEEE Signal Process Lett. 17 (1) (2010) 91–94.
[33] G. Wang, Y. Chen, X. Zheng, Gaussian field consensus: a robust nonparametric matching method for outlier rejection, Pattern Recognit. 74 (2018) 305–316.
[34] B. Qin, Z. Shen, Z. Zhou, J. Zhou, Y. Lv, Structure matching driven by joint-saliency-structure adaptive kernel regression, Appl. Soft Comput. 46 (2016) 851–867.
[35] S. Zhang, K. Yang, Y. Yang, Y. Luo, Z. Wei, Non-rigid point set registration using dual-feature finite mixture model and global-local structural preservation, Pattern Recognit. 80 (2018) 183–195.
[36] B. Qin, Z. Shen, Z. Fu, Z. Zhou, Y. Lv, J. Bao, Joint-saliency structure adaptive kernel regression with adaptive-scale kernels for deformable registration of challenging images, IEEE Access 6 (2018) 330–343.
[37] X. Chang, Z. Ma, M. Lin, Y. Yang, A.G. Hauptmann, Feature interaction augmented sparse learning for fast kinect motion detection, IEEE Trans. Image Proc. 26 (8) (2017) 3911–3920.
[38] Z. Li, F. Nie, X. Chang, Y. Yang, Beyond trace ratio: weighted harmonic mean of trace ratios for multiclass discriminant analysis, IEEE Trans. Knowled. Data Eng. 29 (10) (2017) 2100–2110.
[39] E.J. Candès, B. Recht, Exact matrix completion via convex optimization, Found. Comput. Math. 9 (6) (2009) 717–772.
[40] H. Ma, G. Dibildox, J. Banerjee, W. Niessen, C. Schultz, E. Regar, T. van Walsum, Layer separation for vessel enhancement in interventional x-ray angiograms using morphological filtering and robust PCA, in: Proceedings of the Workshop on Augmented Environments for Computer-Assisted Interventions, Springer, 2015, pp. 104–113.
[41] L.I. Rudin, S. Osher, E. Fatemi, Nonlinear total variation noise removal algorithm, Phys. D 60 (1–4) (1992) 259–268.
[42] S. Wang, Y. Wang, Y. Chen, P. Pan, Z. Sun, G. He, Robust PCA using matrix factorization for background/foreground separation, IEEE Access 6 (2018) 18945–18953.
[43] B. Madathil, S.N. George, Twist tensor total variation regularized-reweighted nuclear norm based tensor completion for video missing area recovery, Inf. Sci. 423 (2018) 376–397.
[44] J.D. Carroll, J.-J. Chang, Analysis of individual differences in multidimensional scaling via an N-way generalization of "Eckart–Young" decomposition, Psychometrika 35 (3) (1970) 283–319.
[45] R.A. Harshman, Foundations of the PARAFAC procedure: models and conditions for an "explanatory" multi-modal factor analysis, UCLA Work. Pap. Phon. 16 (1970) 84.
[46] L.R. Tucker, Some mathematical notes on three-mode factor analysis, Psychometrika 31 (3) (1966) 279–311.
[47] G. Ely, S. Aeron, N. Hao, M.E. Kilmer, 5D and 4D pre-stack seismic data completion using tensor nuclear norm (TNN), in: SEG Technical Program Expanded Abstracts 2013, Society of Exploration Geophysicists, 2013, pp. 3639–3644.
[48] K. Braman, Third-order tensors as linear operators on a space of matrices, Linear Alg. Appl. 433 (7) (2010) 1241–1253.
[49] M.E. Kilmer, K. Braman, N. Hao, R.C. Hoover, Third-order tensors as operators on matrices: a theoretical and computational framework with applications in imaging, SIAM J. Matrix Anal. Appl. 34 (1) (2013) 148–172.
[50] Z. Zhang, G. Ely, S. Aeron, N. Hao, M. Kilmer, Novel methods for multilinear data completion and de-noising based on tensor-SVD, in: Proceedings of the IEEE Conference on Computer Vision and Pattern Recognition, 2014, pp. 3842–3849.
[51] C. Lu, J. Feng, Y. Chen, W. Liu, Z. Lin, S. Yan, Tensor robust principal component analysis: Exact recovery of corrupted low-rank tensors via convex optimization, in: Proceedings of the IEEE Conference on Computer Vision and Pattern Recognition, 2016, pp. 5249–5257.
[52] W. Hu, D. Tao, W. Zhang, Y. Xie, Y. Yang, The twist tensor nuclear norm for video completion, IEEE Trans. Neural Netw. Learn. Syst. 28 (12) (2017) 2961–2973.
[53] I.B. Irrera Paolo, M. Delplanque, A flexible patch based approach for combined denoising and contrast enhancement of digital X-ray images, Med. Image Anal. 28 (2016) 33–45.
[54] F. Zhu, B. Qin, W. Fen, H. Wang, S. Huang, Y. Lv, Y. Chen, Reducing poisson noise and baseline drift in X-ray spectral images with bootstrap poisson regression, Phys. Med. Biol. 58 (6) (2013) 1739–1758.
[55] Q. Zhao, D. Meng, Z. Xu, W. Zuo, L. Zhang, Robust principal component analysis with complex noise, in: Proceedings of the International Conference on Machine Learning, 2014, pp. 55–63.
[56] K. Guo, L. Liu, X. Xu, D. Xu, D. Tao, GoDec+: fast and robust low-Rank matrix decomposition based on maximum correntropy, IEEE Trans. Neural Netw. Learn. Syst. 29 (6) (2018) 2323–2336.
[57] W. Zhao, Y. Lv, Q. Liu, B. Qin, Detail-preserving image denoising via adaptive clustering and progressive PCA thresholding, IEEE Access 6 (2018) 6303–6315.
[58] D. Pandey, X. Yin, H. Wang, Y. Zhang, Accurate vessel segmentation using maximum entropy incorporating line detection and phase-preserving denoising, Comput. Vis. Image Und. 155 (2017) 162–172.
[59] S. Albarqouni, F. Javad, N. Nassir, X-ray in-depth decomposition: revealing the latent structures, in: Proceedings of the International Conference on Medical Image Computing and Computer-Assisted Intervention, Springer, 2017, pp. 444–452.
[60] Z. Lin, M. Chen, Y. Ma, The augmented lagrange multiplier method for exact recovery of corrupted low-rank matrices, arXiv preprint arXiv:1009.5055 (2010).
[61] N. Phansalkar, S. More, A. Sabale, M. Joshi, Adaptive local thresholding for detection of nuclei in diversity stained cytology images, Proceedings of the ICCSP International Conference on Communications and Signal Processing (2011) 218–220.
[62] N. Otsu, A threshold selection method from gray-level histograms, IEEE Trans. Syst. Man, Cybern. 9 (1) (1979) 62–66.
[63] C. Lu, J. Feng, Y. Chen, W. Liu, Z. Lin, S. Yan, Tensor robust principal component analysis with a new tensor nuclear norm, arXiv preprint arXiv:1804.03728 (2018).
[64] T.G. Kolda, B.W. Bader, Tensor decompositions and applications, SIAM Rev. 51 (3) (2009) 455–500.
[65] S. Boyd, N. Parikh, E. Chu, B. Peleato, J. Eckstein, Distributed optimization and statistical learning via the alternating direction method of multipliers, Found. Trends. Mach. Learn. 3 (1) (2011) 1–122.
[66] A. Sobral, E. hadi Zahzah, Matrix and tensor completion algorithms for background model initialization: a comparative evaluation, Pattern Recognit. Lett. 96 (2017) 22–33.
[67] N. Baka, C.T. Metz, C.J. Schultz, R.-J. van Geuns, W.J. Niessen, T. van Walsum, Oriented gaussian mixture models for nonrigid 2D/3D coronary artery registration, IEEE Trans. Med. Image 33 (5) (2014) 1023–1034.
[68] N. Wang, T. Yao, J. Wang, D.-Y. Yeung, A probabilistic approach to robust matrix factorization, in: Proceedings of the European Conference on Computer Vision, Springer, 2012, pp. 126–139.
[69] Y. Cherapanamjeri, K. Gupta, P. Jain, Nearly-optimal robust matrix completion, arXiv preprint arXiv:1606.07315 (2016).
[70] Y. Xu, W. Yin, Z. Wen, Y. Zhang, An alternating direction algorithm for matrix completion with nonnegative factors, Front. Math. China 7 (2) (2012) 365–384.
[71] T. Ngo, Y. Saad, Scaled gradients on Grassmann manifolds for matrix completion, in: Proceedings of the Advances in Neural Information Processing Systems, 2012, pp. 1412–1420.
[72] J. Liu, P. Musialski, P. Wonka, J. Ye, Tensor completion for estimating missing values in visual data, IEEE Trans. Pattern Anal. Mach. Intell. 35 (1) (2013) 208–220.
[73] A. Sobral, T. Bouwmans, E.-h. Zahzah, LRSLibrary: low-rank and sparse tools for background modeling and subtraction in videos, Robust Low-Rank and Sparse Matrix Decomposition: Applications in Image and Video Processing, CRC Press, Taylor and Francis Group, 2016.
[74] C. Tyler, A Novel Retinal Blood Vessel Segmentation algorithm for Fundus Images, MATLAB Central File Exchange, 2016.
[75] B. Felfelian, H.R. Fazlali, N. Karimi, S.M. Soroushmehr, S. Samavi, B. Nallamothu, K. Najarian, Vessel segmentation in low contrast X-ray angiogram images, Proceedings of the International Conference on Image Processing, ICIP (2016) 375–379.
[76] A. Kerkeni, A. Benabdallah, A. Manzanera, M.H. Bedoui, A coronary artery segmentation method based on multiscale analysis and region growing, Comput. Med. Image Gr. 48 (2016) 49–61.
[77] P. Ambrosini, D. Ruijters, W.J. Niessen, A. Moelker, T.v. Walsum, Fully automatic and real-time catheter segmentation in X-Ray fluoroscopy, in: Proceedings of

the International Conference on Medical Image Computing and Computer-Assisted Intervention, 10434, Springer, 2017, pp. 577–585.
[78] P. Liskowski, K. Krawiec, Segmenting retinal blood vessels with deep neural networks, IEEE Trans. Med. Image 35 (11) (2016) 2369–2380.
[79] S. Almasi, A. Ben-Zvi, B. Lacoste, C. Gu, E.L. Miller, X. Xu, Joint volumetric extraction and enhancement of vasculature from low-SNR 3D fluorescence microscopy images, Pattern Recognit. 63 (2017) 710–718.
[80] S. Javed, A. Mahmood, T. Bouwmans, S.K. Jung, Background–foreground modeling based on spatiotemporal sparse subspace clustering, IEEE Trans. Image Proc. 26 (12) (2017) 5840–5854.
[81] J. Fan, T.W. Chow, Non-linear matrix completion, Pattern Recognit. 77 (2018) 378–394.
[82] M. Brbić, I. Kopriva, Multi-view low-rank sparse subspace clustering, Pattern Recognit. 73 (2018) 247–258.
[83] J. Gu, Z. Wang, J. Kuen, L. ma1 Thjh0 TD 0 Tc ( )Tj 524 1 Tf .0044 0 TD (,)Tj /F2 1 Tf .2343 0 TD ( )Tj /F1 1 Tf .3487 0 TD .0007 Tc (L.)Tj /F2 1 Tf .9146 0 TD 0 Tc ( )Tj /F1